

# Hydrothermal Sm-doped tungsten oxide vertically plate-like array photoelectrode and its enhanced photoelectrocatalytic efficiency for degradation of organic dyes

Qiong Liu<sup>1</sup> · Yang Liu<sup>1</sup> · Chang Li<sup>1</sup> · Jie Li<sup>1,3</sup> · Haizhou He<sup>1</sup> · Yaomin Li<sup>4</sup> · Wenzhang Li<sup>1,2,3</sup>

Received: 23 September 2016 / Accepted: 2 November 2016 / Published online: 16 November 2016  
© Springer Science+Business Media New York 2016

**Abstract** Samarium doped tungsten oxide film was synthesized by a hydrothermal method with sodium tungstate as W precursor and samarium oxide as dopant. After annealing at 450 °C for 0.5 h, the morphology and structural characterization of as-prepared films were determined with scanning electron microscopy, X-ray diffraction and high-resolution transmission electron microscope. For the pure and Sm-doped WO<sub>3</sub> films serving as the photoanodes, photoelectrocatalytic properties were demonstrated by degrading methyl orange and methylene blue solution, showing that Sm-doped WO<sub>3</sub> film has faster degrading rate than pure WO<sub>3</sub> film. Photoelectrochemical properties were investigated using linear sweep voltammetry, electrochemical impedance spectroscopy, Mott–Schottky and incident photon to current conversion efficiency. Sm-doped WO<sub>3</sub> achieves a high photocurrent of 1.50 mA cm<sup>-2</sup> at 1.4 V versus. Ag/AgCl, which is 1.8 times as high as that of pure WO<sub>3</sub> film (0.83 mA cm<sup>-2</sup>). Moreover,

photogenerated hole injection efficiency was improved by retarding the recombination at the interface of electrode/electrolyte. The results indicate the Sm<sub>2</sub>O<sub>3</sub> formed by excess doping led to a better photoelectrocatalytic and photoelectrochemical activities of Sm-doped WO<sub>3</sub> film, suggesting that the doping of Sm is a favorable strategy to improve the performance of WO<sub>3</sub> film photoanode.

## 1 Introduction

Tungsten trioxide (WO<sub>3</sub>) has been the focus of extensive research for semiconductor materials because of its superior photoelectrocatalytic properties, low-toxic, excellent reactivity and high photocorrosion resistance [1, 2]. It has a better hole mobility (10 cm<sup>2</sup> V<sup>-1</sup> s<sup>-1</sup>) and a more moderate hole diffusion length (150 nm) compared with α-Fe<sub>2</sub>O<sub>3</sub> (10<sup>-2</sup>–10<sup>-1</sup> cm<sup>2</sup> V<sup>-1</sup> s<sup>-1</sup> and 2–20 nm) and TiO<sub>2</sub> (100 nm), which shows the inherently good electron transport properties [3–6]. However, there are still some deficiencies which limited the use of WO<sub>3</sub> thin-film photoanode as photoelectrocatalytic material. The first barrier for WO<sub>3</sub> is that the band gap ( $E_g \approx 2.5$ – $2.8$  eV) limits the photoresponse region in the solar spectrum, which results in the unsatisfactory solar to hydrogen conversion efficiencies of the devices (less than about 5% as experimental validation) [7–10]. Another one is the serious recombination of electrons and holes, which is a common problem for the semiconductor photoanode. To increase the photoelectrocatalytic performance, reducing the recombination of electron-holes pairs of WO<sub>3</sub> and improving the lifetime of photoelectrons are still necessary.

An effective way to improve the photoelectrocatalytic activity is constructing one or two dimensional materials.

Qiong Liu and Yang Liu have contributed equally to this work.

✉ Jie Li  
lijieliu@csu.edu.cn

✉ Wenzhang Li  
liwenzhang@csu.edu.cn

- <sup>1</sup> School of Chemistry and Chemical Engineering, Central South University, Changsha 410083, China
- <sup>2</sup> Key Laboratory of Metallogenic Prediction of Nonferrous Metals and Geological Environment Monitoring (Central South University), Ministry of Education, Changsha 410083, China
- <sup>3</sup> Key Laboratory of Hunan Province for Metallurgy and Material Processing of Rare Metals, Changsha 410083, China
- <sup>4</sup> Department of Chemistry, University College London, London WC1H 0AJ, UK

Compared with the nanocrystal film, the nanostructural film (such as  $\text{WO}_3$  plate-like arrays film) provides a more useful method to achieve high photocurrent. Mallouk et al. [11] reported a route to fabricate vertically aligned  $\text{WO}_3$  nanoparticulate flakes with high surface area and sufficient film thickness for good light absorption. Su et al. [12] synthesized vertically aligned  $\text{WO}_3$  nanowire and nanoflake arrays by the solvothermal technique, and they showed high photocurrent and efficient charge transfer. Joo et al. [13] demonstrated a facile hydrothermal method to grow oriented  $\text{WO}_3$  nanorods on fluorine-doped tin oxide (FTO), which provided the direct pathway for charge transfer. Wang et al. [14] reported a facile hydrothermal method for growing  $\text{WO}_3$  nanoplate arrays with (002) oriented facets on FTO. Sun et al. and Li et al. [15–17] also synthesized vertically plate-like  $\text{WO}_3$  arrays by hydrothermal method. The results of above literature demonstrated that one or two dimensional nanostructure film exhibits a high surface area, unique morphology and efficient charge transfer by providing the direct pathway.

Furthermore, some strategies, such as coupled with cocatalysts [18–23], doped with metal or nonmetal elements [24–29] and modified with noble metals [30, 31], have also been taken into consideration by numerous researchers. Besides, surface modification of semiconductor photoanodes with passivation overlayers was introduced to PEC, with the aim of improving the charge separation and charge-transfer processes across the semiconductor–electrolyte interface.

For example, Sivula et al. [32] said that an  $\text{Al}_2\text{O}_3$  overlayer deposited using atomic layer deposition (ALD) decreases the overpotential required for water oxidation on hematite due to the passivation of surface trapping states. Yang et al. [33] reported the effect of ultrathin  $\text{TiO}_2$  deposition prepared using the ALD method on the performance of hematite photoanodes. Li et al. [34] passivated the surface states of one-dimensional anodic titanium oxide nanotube by coating with an  $\text{Al}_2\text{O}_3$  layer using ALD. For  $\text{WO}_3$ ,  $\text{Al}_2\text{O}_3$  overlayer as a passivation layer was loaded on the surface of  $\text{WO}_3$  by atomic layer deposition, which facilitated the photoelectron transfer to the external circuit in the presence of a positive bias. Yang et al. [35] reported  $\text{WO}_3$  vertically plate-like arrays were covered with  $\text{HfO}_2$  overlayers, enhancing the photoelectrochemical properties by inhibiting the recombination of electrons and holes at the interface of electrode/electrolyte. In addition, Fujishima et al. said that Gd ion doping had the effect on bottlenecking of photoelectrons trapping at surface states of  $\text{TiO}_2$ . It means that surface doping with high ionic radii rare earth metals can not only modify the bandgap, but also inhibit the recombination of electrons and holes at the interface of electrode/electrolyte. Although several earlier papers have explained the advantages of the rare earth ion

doped semiconductor particles in promoting photocatalytic activity, the photoelectrocatalytic mechanism in the form of film electrode still need a further investigation [36–38]. In this paper, Sm-doped tungsten trioxide film was prepared by hydrothermal method with sodium tungstate as W precursor and samarium oxide as dopant. The photoelectrocatalytic ability and corresponding photoelectrochemical properties of Sm doped  $\text{WO}_3$  nanoplates film were investigated in detail using the degradation of MO and MB. The study of the mechanisms is applied with linear sweep voltammetry (LSV), electrochemical impedance spectroscopy (EIS), Mott–Schottky, incident photon to current conversion efficiency (IPCE) and injection efficiencies ( $\eta_{inj}$ ). The role of Sm in the enhanced photoelectrocatalytic ability of  $\text{WO}_3$  is also discussed.

## 2 Experimental section

### 2.1 Preparation of nanostructured films

All chemicals were of analytical grade and were used without further purification. Tungsten oxide thin film was synthesized by hydrothermal method with sodium tungstate as precursor and ammonium oxalate as the assistant agent [16, 39, 40]. In a typical procedure, dispersing 0.231 g  $\text{Na}_2\text{WO}_4$  into 30 mL deionized (DI) water, and the samarium oxide (0.010 g) was added at the same time. Then 6 mL of 3 M HCl was added dropwise to the solution with magnetic stirring for 10 min. 0.200 g  $(\text{NH}_4)_2\text{C}_2\text{O}_4$  was added with additional stirring for 20 min. Afterwards, 34 mL DI water was added to the solution and stirred for 5 min. The mixture was transferred to a 100 mL Teflon-lined stainless steel autoclave with two clean FTO glasses ( $2 \times 3 \text{ cm}^2$ ) in an oblique position against the wall. The whole system was moved to the oven under 120 °C for 12 h after being sealed and then cooling to room temperature. The films were taken out, washed with DI water and absolute alcohol respectively and placed in the oven under 60 °C for 30 min. Finally, the films were placed in combustion boat and annealed at 450 °C for 1 h under air atmosphere with a heating rate of 2 °C  $\text{min}^{-1}$ , which is donated as Sm– $\text{WO}_3$ . For comparison, the pure  $\text{WO}_3$  is fabricated in the same way without adding the  $\text{Sm}_2\text{O}_3$ .

### 2.2 Characterizations

X-ray diffraction (XRD) was used to characterize the crystalline phases of all the samples in the range of 15°–70° with a step width of 0.02° and the scanning rate of 10°  $\text{min}^{-1}$  using Cu K $\alpha$  radiation (D/Max 2250, Rigaku Corporation, Japan). Scanning electron microscopy (SEM, JSM6700F, JEOL Company, Japan) was applied to observe

the surface and cross-sectional morphology as well as particle sizes. High-resolution transmission electron microscope (HRTEM, TECNAIG2 F20, FEI, Japan) was operated at 200 kV to investigate the microstructure. UV–Vis spectra of the film photoanodes, in the range of 400–530 nm, was obtained with a spectrophotometer (PGeneral TU-1901). X-ray photoelectron spectrograph (XPS, ESCALAB250Xi, ThermoFisher-VG Scientific) was recorded for the chemical composition and the valence states of Sm–WO<sub>3</sub>.

### 2.3 Photoelectrocatalytic measurements

The detection of photoelectrocatalysis performance was measured using a standard three-electrode system with platinum foil as a counter electrode, Ag/AgCl (saturated KCl) as a reference electrode, and pure WO<sub>3</sub> or Sm–WO<sub>3</sub> films electrode ( $2 \times 1.5 \text{ cm}^2$ ) as the photoanode. In order to determinate photoelectrocatalytic activities, the photoanode was immersed in a 80 mL methyl orange solution (MO  $15 \text{ mg L}^{-1}$  and 0.5 M NaCl), which is adjusted to pH = 4 by 3 M H<sub>2</sub>SO<sub>4</sub>. The mixture was placed for 15 min in the dark to reach the adsorption–desorption equilibrium. Irradiation of photoanode by 500 W xenon lamp from the backside of FTO, and the photoanode was at the potential of 0.8 V (vs. Ag/AgCl). 1 mL solution was taken out at a given time for analysis. Methylene blue solution (MB  $10 \text{ mg L}^{-1}$  and 0.5 M NaCl) was also degraded in the same method. The solution samples were analyzed by recording variations in the absorption of the UV–Vis spectra for MO and MB using an ultraviolet spectrophotometer (UV-1081).

### 2.4 Photoelectrochemical measurements

Photoelectrochemical measurements were performed on a Zahner electrochemical workstation (Zennium, Zahner, Germany) using standard three-electrode system with platinum foil as a counter electrode, Ag/AgCl (saturated KCl) as a reference electrode, pure WO<sub>3</sub> or Sm–WO<sub>3</sub> nanoplate electrode ( $1 \times 1.5 \text{ cm}^2$ ) as the photoanode, and 0.2 M Na<sub>2</sub>SO<sub>4</sub> solution as electrolyte solution. The Linear sweep voltammetry (LSV) were used for photocurrents characterization with potential range from  $-0.05$  to  $1.4 \text{ V}$  (vs. Ag/AgCl) and scan rate of  $20 \text{ mV s}^{-1}$  under AM 1.5G illumination. The electrochemical impedance spectroscopy (EIS) was measured under potential of  $0.6 \text{ V}$  (vs. Ag/AgCl), with an alternating voltage (AC) perturbation of  $10 \text{ mV}$ , and the AC frequency was from  $10 \text{ kHz}$  to  $0.1 \text{ Hz}$ . The Mott–Schottky plots were measured at an AC frequency of  $1 \text{ kHz}$ . The incident photon to current conversion efficiency (IPCE) of the photoelectrodes were measured at a bias voltage of  $1.2 \text{ V}$  in  $0.2 \text{ M Na}_2\text{SO}_4$  solution.

## 3 Results and discussion

### 3.1 Morphology and structure characterization

XRD patterns were employed to detect the structural properties. The diffraction peaks for both pure WO<sub>3</sub> and Sm–WO<sub>3</sub> nanoplates are shown in Fig. 1. The significant diffraction peaks ( $23.12^\circ$ ,  $28.91^\circ$ ,  $33.70^\circ$ ,  $34.15^\circ$ ,  $41.95^\circ$ ,  $51.53^\circ$  and  $55.98^\circ$ ) can be observed, which is assigned to monoclinic WO<sub>3</sub> (JCPDS no. 72-0677). Monoclinic WO<sub>3</sub> is the most common crystal form and has fairly good chemical stability [41]. There are also some diffraction peaks ( $26.54$ ,  $33.80$ ,  $37.85$ ,  $51.88$ ) corresponding to tetragonal SnO<sub>2</sub> (JCPDS no. 46-1088), suggesting that both samples are loaded on FTO. The refinement of XRD data shows a slightly change of lattice parameters (Table 1). The slight increase of the cell volume may caused by the larger atomic ( $1.80 \text{ \AA}$ ) [42, 43] and ionic radii ( $0.964 \text{ \AA}$ ) [44] of Sm than that of W ( $1.370$ ,  $0.60 \text{ \AA}$ ) [45, 46], indicating that the few Sm has been doped in the unit cell [47].

The chemical composition of Sm–WO<sub>3</sub> and the valence states of various species were determined by X-ray photoelectron spectroscopy. Figure 2 shows the XPS patterns of Sm–WO<sub>3</sub> thin film. In Fig. 2a, only peaks assigned to Sm, O, W and C electrons were identified. The peaks around  $1090 \text{ eV}$  are corresponding to Sm 3d peaks, certifying the doping of Sm in WO<sub>3</sub> nanomaterials [48]. The peaks at  $530.4$  and  $37.5 \text{ eV}$  can be assigned to the O 1s and

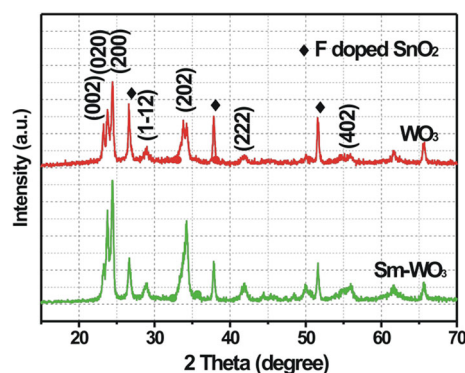
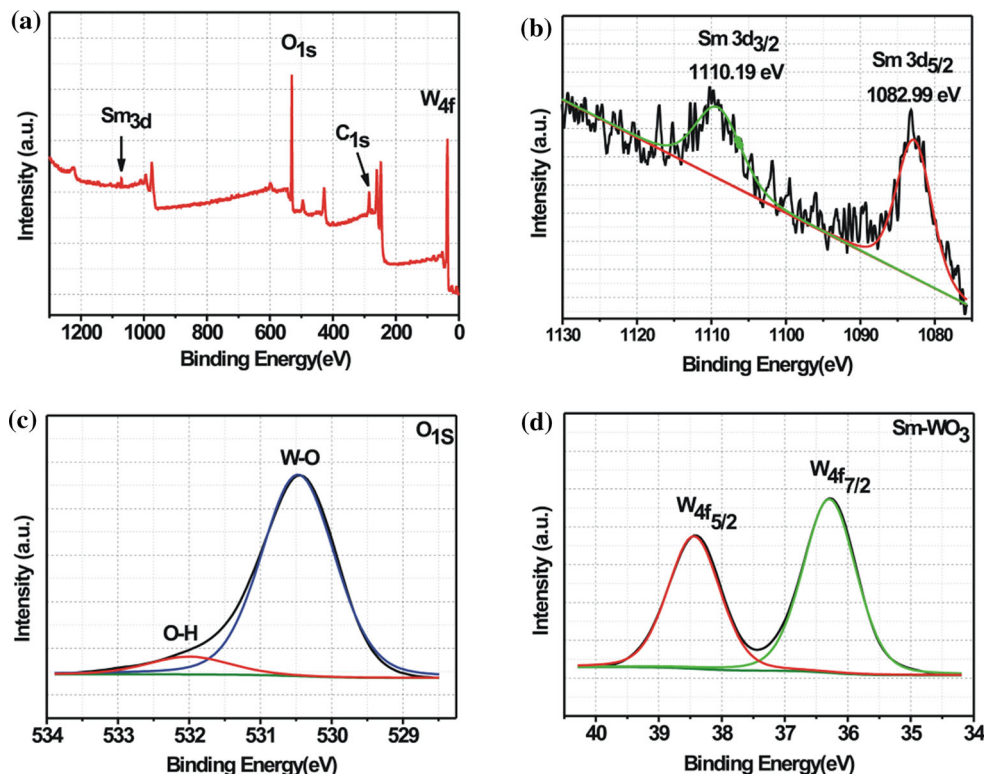


**Fig. 1** XRD patterns of pure WO<sub>3</sub> and Sm–WO<sub>3</sub> nanoplate

**Table 1** Lattice parameters a, b, c, beta angle ( $\beta$ ), and the cell volume of pure WO<sub>3</sub> and Sm–WO<sub>3</sub>

Sample	Pure WO <sub>3</sub>	Sm–WO <sub>3</sub>
a ( $\text{\AA}$ )	7.30204	7.3039
b ( $\text{\AA}$ )	7.53464	7.539
c ( $\text{\AA}$ )	7.63805	7.63771
$\beta$ ( $^\circ$ )	90.581	90.594
V ( $\text{\AA}^3$ )	420.378	420.542

**Fig. 2** The XPS spectra of Sm–WO<sub>3</sub> nanoplate film: **a** XPS entire spectrum, **b** Sm 3d, **c** XPS O 1s and **d** XPS W 4f



W 4f, respectively [18, 49, 50]. Moreover, the C 1s peak at 284.8 eV is due to the adventitious carbon species such as organic groups ((CH<sub>2</sub>)<sub>n</sub>) or molecules of the XPS instrument [51–53]. In the XPS Sm 3d spectrum (Fig. 2b), two peaks observed at binding energies of 1110.19 and 1082.99 eV are corresponding to Sm 3d 3/2 and Sm 3d 5/2, respectively, which confirmed the existence of Sm in the Sm–WO<sub>3</sub> nanoplates [54]. In the O 1s region (Fig. 2c), the peak at 530.7 and 532.0 eV can be assigned to oxygen atoms in the tungsten oxide (W–O) and surface hydroxyl oxygen (O–H) [19]. Jung et al. [55] reported that the interfacial O–H can achieve greatly enhanced PEC water oxidation activity. Figure 2d shows the XPS W 4f spectra of Sm–WO<sub>3</sub> films, and the two peaks at the binding energies of 36.29 and 38.44 eV are corresponding to the deconvoluted W 4f 7/2 and W 4f 5/2 peaks, respectively [56, 57].

To study the surface configuration of pure WO<sub>3</sub> nanoplates and the Sm–WO<sub>3</sub> nanoplates films, SEM micrographs were measured and shown in Fig. 3. In Fig. 3a, it can be seen that pure WO<sub>3</sub> film exhibits highly dense and uniform vertical nanoplates, and the average height of film is approximately 1.7 μm (inset of Fig. 3a). For the Sm–WO<sub>3</sub> nanoplates film (Fig. 3b), the surface is relatively rough and the average size of nanoplates is increased compared with the pure one, which may provide the more bonding sites of oxidizing reaction. Meanwhile, the average height has no obvious change. To further investigate

more details of the microstructure of the samples, high-resolution transmission electron microscope (HRTEM) image (Fig. 3c) of the Sm–WO<sub>3</sub> was recorded. The lattice fringes of the two different area in the HRTEM are shown in the inset of Fig. 3c. The lattice spacing of blue square area of the HRTEM is 0.359 nm, corresponding to the (2 0 0) plane of monoclinic WO<sub>3</sub> (JCPDS no. 72-0677). The lattice spacing of the red square area was 0.229 nm, corresponding to the (4 2 2) plane of cubic samarium oxide (JCPDS no. 42-1461). It is because that the content of Sm exceeds the solubility limit for WO<sub>3</sub>, and the excessive Sm atoms exist as samarium oxide [58]. Recently, Sudhagar et al. have reported the similar phenomenon that the lattice fringe of pure Gd<sub>2</sub>O<sub>3</sub> was found in the Gd<sup>3+</sup> doped TiO<sub>2</sub>, and they considered Gd<sup>3+</sup> ions are occupied at the grain boundaries of TiO<sub>2</sub> clumps [59]. This external layer is suggested with passivation of recombination route of photoelectrons and holes.

### 3.2 Optical characteristic

The UV–Vis absorbance spectra of both undoped WO<sub>3</sub> and Sm doped WO<sub>3</sub> films scanning from 400 to 530 nm were shown in Fig. 4. The light absorption edge of the undoped WO<sub>3</sub> is about 466 nm, which is in accordance with the band gap energy of 2.63 eV. After samarium doping, the absorption edge increases from 471 to 479 nm, corresponding to the band gap energy of 2.59 eV. It can be

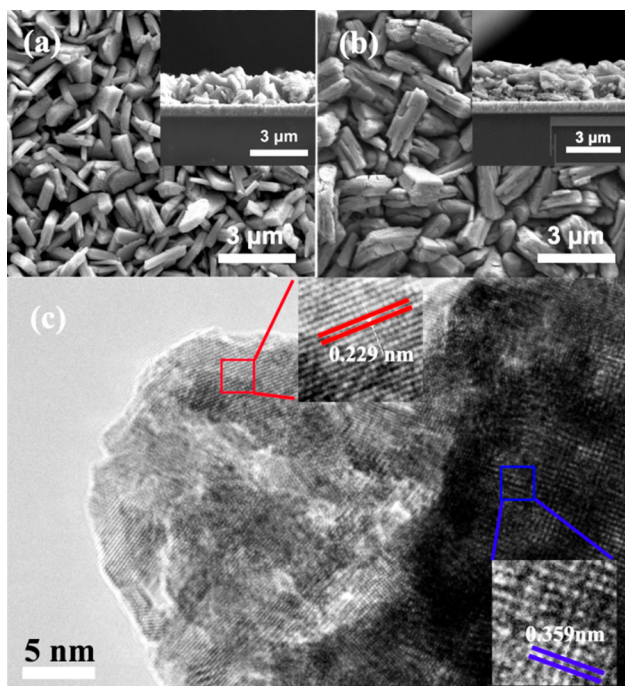


**Fig. 3** SEM images **a**  $\text{WO}_3$  nanoplate film and **b**  $\text{Sm-WO}_3$  nanoplate film **c** high-resolution transmission electron microscope (HRTEM) of the  $\text{Sm-WO}_3$

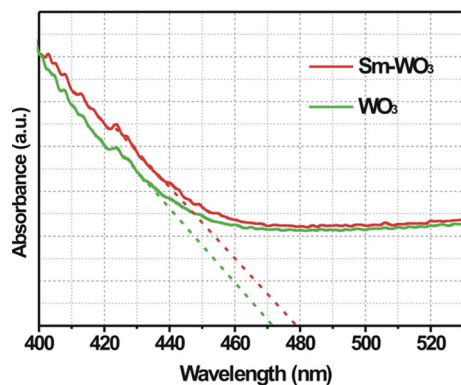


**Fig. 4** UV-Vis absorbance spectroscopy of  $\text{WO}_3$  and  $\text{Sm-WO}_3$

explained by the orbital overlap of O 2p and Sm 4f/5d, which causes the formation of conjugated structure [60, 61]. The slight change of bandgap is due to the limited doping volume caused by the large ionic radius of  $\text{Sm}^{3+}$ . It is similar with Yang et al. result [62], in which the bandgap of  $\text{WO}_3$  decrease from 2.60 to 2.51 eV after doping of Fe element. Moreover, the absorbance of  $\text{Sm-WO}_3$  in the region of 480–530 nm is marginally higher than that of  $\text{WO}_3$ . It is because that the surface of  $\text{WO}_3$  nanoplates may be covered by  $\text{Sm}_2\text{O}_3$ .

### 3.3 Photoelectrocatalysis performance

We compared the photocatalytic activity of the  $\text{Sm-WO}_3$  film with that of the  $\text{WO}_3$  film by taking the decomposition of MO as a model reaction. Both the samples immersed in electrolyte solution and stirred in the dark for 10 min before visible-light irradiation to reach basically adsorption equilibrium. Figure 5b shows the temporal evolution of the spectral changes during the photodegradation of MO by  $\text{WO}_3$  film, which is continuously decreasing in intensity with reaction time. The characteristic absorption peak is at about 504 nm, which depends on the solution pH [63]. He et al. reported that the adsorption of methyl orange will be gradually increased on the surface of  $\text{WO}_3$  film with decreasing pH value [2]. The increased adsorption could favor the removal of methyl orange. In Fig. 5a, the spectral changes of degradation of MO by  $\text{Sm-WO}_3$  film show a significant decrease, indicating that MO molecules are completely decomposed after the reaction for 3 min. In contrast, decomposition of the same amount of MO requires about 5 min when  $\text{WO}_3$  film is used as catalyst. In Fig. 5c, plots of the degradation ratio in the presence of different catalysts under irradiation were obtained, where  $C/C_0$  is the ratio between the concentration of the MO ( $C$ ) under different irradiation time and the concentration of the MO prior to the decomposition reaction ( $C_0$ ). As a comparison, the MO solution without addition of photoelectrocatalysts was measured (Fig. 5c), and the catalytic activity of  $\text{Sm-WO}_3$  film without irradiation was also detected. Both of the two measurements show negligible degradation of MO. The reaction kinetics can be plotted in the natural logarithm of the ( $C_0/C$ ) as a function of the reaction time ( $t$ ). As highlighted in Fig. 5d, the relationship exhibits a linear dependence before the MO is decomposed completely, indicating that the photoelectrocatalytic decomposition reaction follows first-order kinetics:  $-\ln(C/C_0) = kt$  where  $k$  is the degradation rate constant [64]. From the slopes of the fitted straight lines, the values of  $k$  are 0.959 and  $1.202 \text{ min}^{-1}$  for the reactions with  $\text{WO}_3$  film and  $\text{Sm-WO}_3$  film as catalysts, respectively, indicating the better photocatalytic ability of the  $\text{Sm-WO}_3$  film than that of the  $\text{WO}_3$  film. Figure 6a shows the degradation ratio after lighting versus reaction time for the decomposition of MB. After irradiation of 15 min,  $\text{Sm-WO}_3$  film degraded  $\sim 91\%$  MB, while  $\text{WO}_3$  film degraded  $\sim 35\%$ . In Fig. 6b, the fitted degradation rate constants are 0.029 and  $0.146 \text{ min}^{-1}$  for the reactions with  $\text{WO}_3$  film and  $\text{Sm-WO}_3$  film, respectively. Both reactions of degrading MO and MB have proved that Sm doped  $\text{WO}_3$  shows the much better photoelectrocatalytic decomposition efficiency than pure  $\text{WO}_3$  film.

**Fig. 5** Photoelectrocatalytic degradation of MO using **a** Sm-WO<sub>3</sub> nanoplates film and **b** WO<sub>3</sub> film. **c** the degradation of MO in absence/presence of WO<sub>3</sub> or Sm-WO<sub>3</sub> film under irradiation and degradation of MO in dark. **d**  $-\ln(C/C_0)$  versus time curves

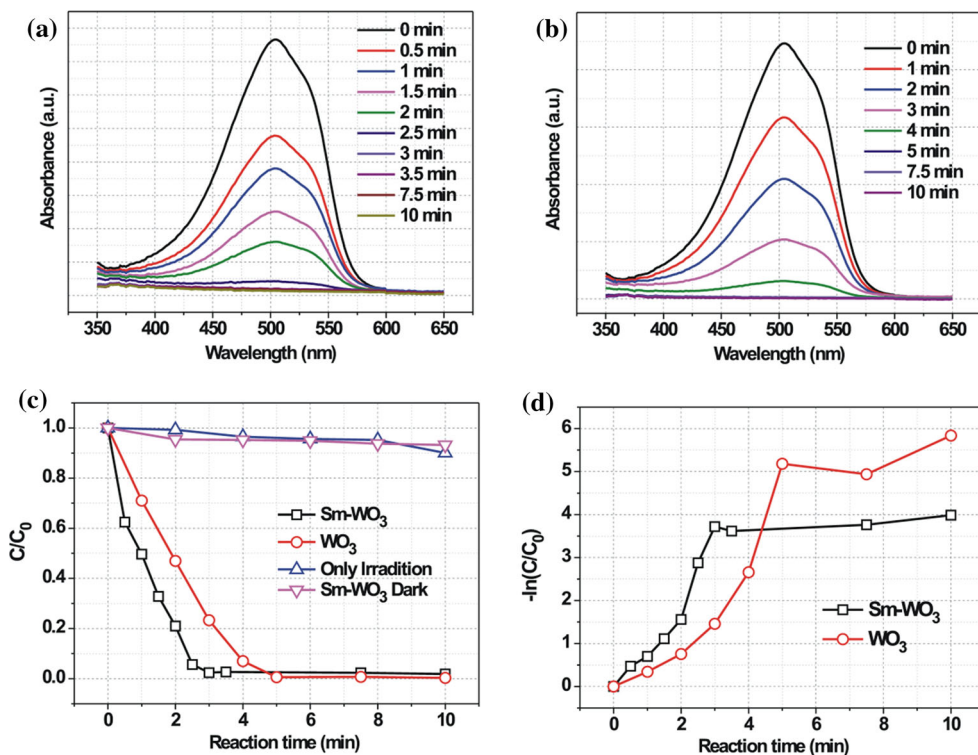
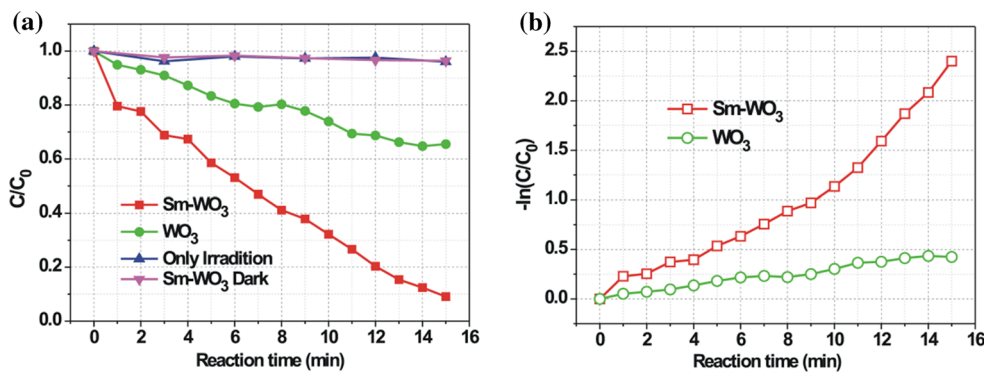


**Fig. 6** **a** The degradation of MB in absence/presence of WO<sub>3</sub> or Sm-WO<sub>3</sub> film under irradiation and degradation of MB in dark. **b**  $-\ln(C/C_0)$  versus time curves



### 3.4 Photoelectrochemical property

Generally, light absorption ability, surface properties and photogenerated charge separation efficiency are three crucial important factors of photocatalytic activity [65]. From the UV-Vis analysis, it can be found that the change of light absorption ability is slight. To further study the possible reasons for the enhancement of photocatalytic activity, several photoelectrochemical measurements were performed. Linear sweep voltammetry (LSV) scans of undoped and Sm doped WO<sub>3</sub> films were detected under illumination or in the dark condition. In Fig. 7, the photocurrent density of the pure WO<sub>3</sub> is obviously lower than the Sm-WO<sub>3</sub> film under illumination. At the potential of 1.4 V (vs. Ag/AgCl), the observed current density of Sm-WO<sub>3</sub> film is 1.50 mA cm<sup>-2</sup>, which is about 1.8 times as

high as that of pure WO<sub>3</sub> film (0.83 mA cm<sup>-2</sup>). In the dark condition, the current densities of both samples are about

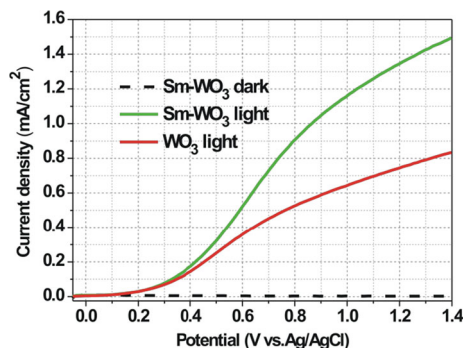


**Fig. 7** Linear sweep voltammetry scans of the undoped and Sm-WO<sub>3</sub> films under illumination and in the dark

zero, indicating that the improved photocurrent is not caused by chemical corrosion or electrocatalysis.

The EIS spectra of  $\text{WO}_3$  and Sm-doped  $\text{WO}_3$  electrode are shown in Fig. 8a. The Nyquist plot was measured under the potential of 0.6 V (vs. Ag/AgCl), with an AC voltage perturbation of 10 mV, and the AC frequency was from 10 kHz to 0.1 Hz. Under irradiation, the radius of Nyquist plot of the Sm- $\text{WO}_3$  electrode is smaller than that of pure  $\text{WO}_3$ , suggesting that the interfacial charge-transfer resistance is decreased after doping of samarium, and the speed of carrier transmission was dramatically improved. The lower impedance also signifies the better photoelectric property of Sm-doped  $\text{WO}_3$  nanoplates film. It may be caused by the passivation of recombination route, where photogenerated holes can flow through the surface states or interface defects to electrolyte so as to retard recombination. Figure 8b is the equivalent electric circuit of electrochemical impedance spectra [66].  $R_s$  represents the resistance of solution acquired from the high frequency region.  $R_{ct}$  reflects the charge transfer resistance between the electrodes and the solution interface, and the related

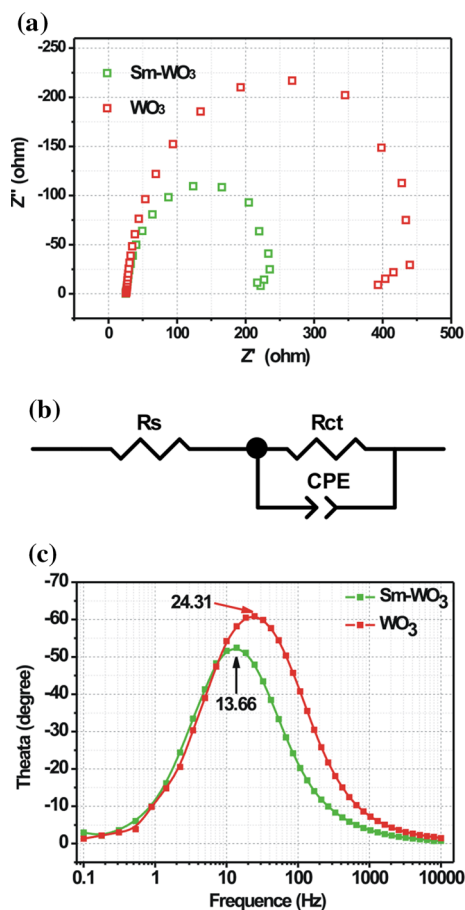


**Fig. 8** **a** The electrochemical impedance spectra of  $\text{WO}_3$  and Sm- $\text{WO}_3$ . **b** The electrochemical impedance spectrum fitting circuit. **c** The bode phase plots of the photoelectrodes

parameters can be obtained from the low frequency region of Nyquist plots. Figure 8c exhibits the bode plots of both undoped and Sm-doped  $\text{WO}_3$  films. As presented in Fig. 8c, the  $f_{\max}$  value of undoped and Sm-doped  $\text{WO}_3$  films is 24.31 and 13.66 Hz, respectively. The electron lifetime ( $\tau$ ) of photo-induced electron are calculated according to the formula [18]:

$$\tau = \frac{1}{2\pi f_{\max}}$$

where  $f_{\max}$  represents the frequency-peak of Nyquist plots. The results are shown in the Table 2. The electron lifetime of Sm-doped nanoplates film (12 ms) is longer than that of pure  $\text{WO}_3$  (6.4 ms). This result further confirms that recombination of photogenerated electrons and holes are inhibited after doping of Sm, which is in favor of extending charge carriers lifetime, subsequently leading to much improved photoelectrocatalytic ability.

The Mott–Schottky measurements were carried out with 1 kHz frequency to obtain flat band potential. In Fig. 9, the slopes of both samples are positive which means the films are n-type semiconductors with electrons as the major carriers. The density of charge carrier depends on the value of the slope of the Mott–Schottky. Compared with the pure  $\text{WO}_3$  film, the Sm-doped  $\text{WO}_3$  film suggests obviously increased donor densities based on the following equation [22]:

$$\frac{1}{C_{sc}^2} = \frac{2}{\epsilon \epsilon_0 e_0 N_d} \left( U - V_{fb} - \frac{kT}{q} \right)$$

where  $e_0$  is the electron charge;  $\epsilon, \epsilon_0$  means the dielectric constant of  $\text{WO}_3$  and permittivity of vacuum, respectively.  $N_d$  is the donor density. The electron densities of pure  $\text{WO}_3$  and Sm- $\text{WO}_3$  film are  $4.986 \times 10^{19} \text{ cm}^{-3}$  and  $1.942 \times 10^{20} \text{ cm}^{-3}$ , respectively, which indicates an increased electron density after Sm doping. By extrapolating the X-intercepts of the liner region in Mott–Schottky plots, the flat band potential ( $V_{fb}$ ) is estimated, and a negative shift of  $V_{fb}$  is obtained for the  $\text{WO}_3$  film after doping. It can be explained by the hybridization of O 2p orbitals with the Sm 4f/5d states which lead to the generation of charge carriers in the form of electrons or holes.

To estimate the injection efficiencies ( $\eta_{inj}$ ) of  $\text{WO}_3$  and Sm- $\text{WO}_3$  film, current–potential curves were measured in

**Table 2** The electron lifetime ( $\tau$ ) and the fitted parameters of undoped and Sm-doped nanoplates  $\text{WO}_3$  photoelectrodes

Sample	Undoped	Sm-doped
Frequency/Hz	24.3	13.7
Time/ms	6.4	12.0
$R_s$ /ohm	26.0	25.7
$R_{ct}$ /ohm	420.8	213.8

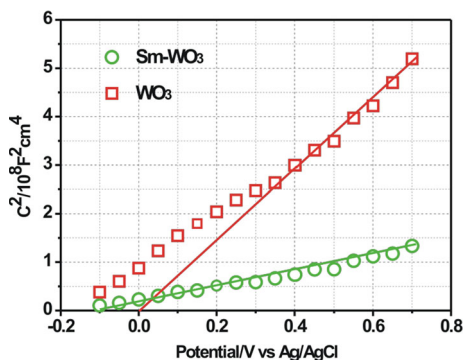


**Fig. 9** Mott–Schottky plots of  $\text{WO}_3$  and  $\text{Sm-WO}_3$

0.5 M potassium phosphate buffer solution ( $\text{pH} \approx 7$ ) with/ without 0.5 M  $\text{H}_2\text{O}_2$ . As shown in Fig. 10a, b,  $\text{Sm-WO}_3$  shows a negative shift of onset potential when compared with pure  $\text{WO}_3$ . It means a negative of  $V_{\text{fb}}$ , which is consistent with the result of Mott–Schottky. When hydrogen peroxide ( $\text{H}_2\text{O}_2$ ) is used as hole scavenger during the measurement, the  $\eta_{\text{inj}}$  is considered as 100% because surface recombination is completely suppressed. Thus, it can be calculated according to the equation:

$$\eta_{\text{inj}} = I_{\text{H}_2\text{O}}/I_{\text{H}_2\text{O}_2}$$

In Fig. 10c, the injection efficiency of  $\text{Sm-WO}_3$  ( $\sim 80\%$ ) is higher than that of pure  $\text{WO}_3$  ( $\sim 73\%$ ). It indicates that the passivation by  $\text{Sm}_2\text{O}_3$  at the surface of  $\text{WO}_3$  plates inhibits the recombination of electrons and hole at the interface of electrode/electrolyte so as to promote photo-generated holes participate in the reaction of water oxidation.

Meanwhile, the incident photon to current conversion efficiency (IPCE) is employed to investigate the effect of samarium doping on the photoelectrocatalytic ability of  $\text{WO}_3$  film. The measurements were conducted at a bias voltage of 1.2 V in 0.2 M  $\text{Na}_2\text{SO}_4$  solution. As shown in Fig. 11, the results are calculated according to the following formula [67]:

$$\text{IPCE} = \frac{1240 \times I}{\lambda \times J_{\text{light}}}$$

where  $I$  is photocurrent density ( $\text{mA cm}^{-2}$ ),  $\lambda$  is the wavelength (nm),  $J_{\text{light}}$  is the power density of incident light ( $\text{mW cm}^{-2}$ ).

It can be seen that the IPCE value of pure  $\text{WO}_3$  drops to zero at wavelengths longer than 460 nm, and the highest is about 23.0% at the wavelength of 350 nm. After doping of Sm, the photoresponse region shift to visible light slightly, corresponding to the result of the UV–Vis diffused reflectance spectroscopy. Meanwhile, IPCE value is improved in the range of 330–470 nm, and the highest value is about 30.5% at the wavelength of 360 nm. It is

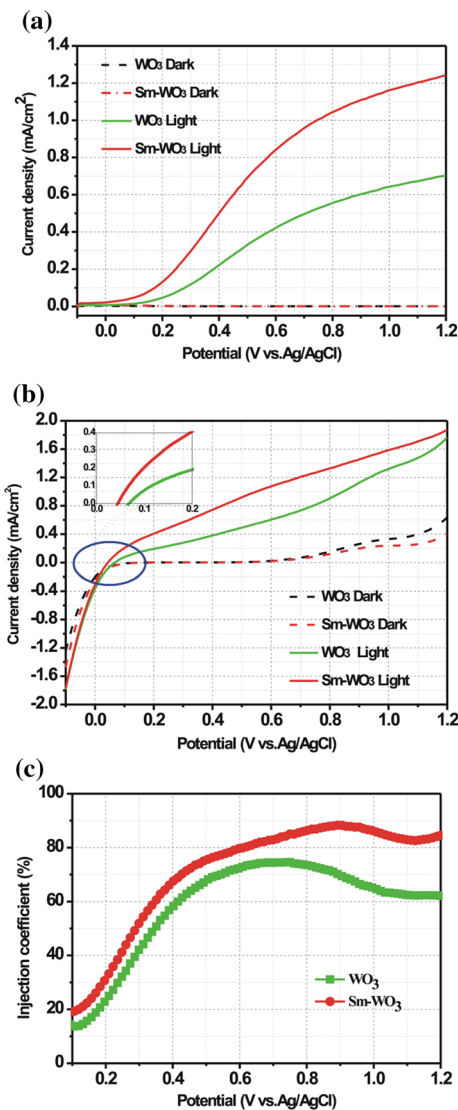


**Fig. 10** Current–potential curves of the undoped and  $\text{Sm-WO}_3$  films under illumination/dark in 0.5 M potassium phosphate buffer solution ( $\text{pH} = 7$ ) **a** without/ **b** with 0.5 M  $\text{H}_2\text{O}_2$ . **c** The injection efficiency of undoped and  $\text{Sm-WO}_3$  films

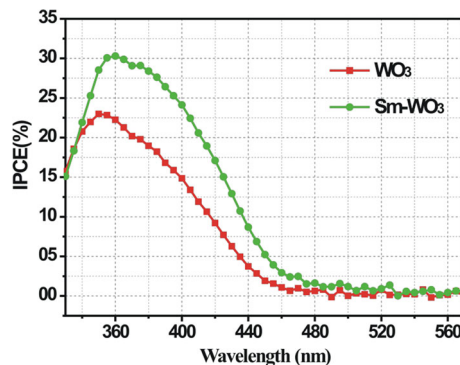


**Fig. 11** Incident photon to current conversion efficiency (IPCE) of pure and Sm doped  $\text{WO}_3$  films



consistent with the result of linear sweep voltammetry scans, suggesting that the Sm–WO<sub>3</sub> film shows a better photoelectrocatalytic activity due to the increased electron lifetime, which is caused by inhibiting recombination of electrons and holes at the interface of electrode/electrolyte.

## 4 Conclusions

In summary, Sm-doped WO<sub>3</sub> film has been synthesised by the hydrothermal method and characterised with a series of electrochemical methods to study the mechanisms of photocatalytic activity enhancement. After modified with Sm, the electron lifetime and the injection efficiency are increased because the recombinations of photogenerated electrons and holes are inhibited, leading to a better photoelectrocatalytic ability for the Sm–WO<sub>3</sub>. Meanwhile, the photodegradation of MB and MO by Sm–WO<sub>3</sub> film under irradiation shows a greater ability in photoelectrocatalysis than the pure WO<sub>3</sub>, and the photocurrent of Sm–WO<sub>3</sub> film is 1.8 times as high as that of the pure WO<sub>3</sub> film. As a semiconductor material with better environmental protection and higher efficiency, the samarium doped tungsten trioxide nanoplates have potential applications for the treatment of dyeing wastewater.

**Acknowledgements** This study was supported by the National Nature Science Foundation of China (No. 51304253), the open research Fund Program of Key Laboratory of Metallogenic Prediction of Nonferrous Metals and Geological Environment Monitoring (Central South University), Ministry of Education, the Fundamental Research Funds for the Central Universities of Central South University (2015zzts021), and Y.L. acknowledges financial support from the China Scholarship Council (CSC File No. 201406370157).

## References

- C.A. Bignozzi, S. Caramori, V. Cristino, R. Argazzi, L. Meda, A. Tacca, *Chem. Soc. Rev.* **42**, 2228–2246 (2013)
- X. Chen, Y. Zhou, Q. Liu, Z. Li, J. Liu, Z. Zou, *ACS Appl. Mater. Interfaces* **4**, 3372–3377 (2012)
- J.E. Yourey, B.M. Bartlett, *J. Mater. Chem.* **21**, 7651–7660 (2011)
- J.Y. Zheng, G. Song, C.W. Kim, Y.S. Kang, *Nanoscale* **5**, 5279 (2013)
- J.Y. Zheng, G. Song, J. Hong, T.K. Van, A.U. Pawar, D.Y. Kim, C.W. Kim, Z. Haider, Y.S. Kang, *Cryst. Growth Des.* **14**, 6057–6066 (2014)
- B. Liu, Y. Xue, J. Zhang, D. Wang, T. Xie, X. Suo, L. Mu, H. Shi, *J. Mater. Sci. Mater. Electron.* **27**, 10213–10220 (2016)
- B. Cole, B. Marsen, E. Miller, Y. Yan, B. To, K. Jones, M. Al-Jassim, *J. Phys. Chem. C* **112**, 5213–5220 (2008)
- J. Desilvestro, M. Graetzel, L. Kavan, J. Moser, J. Augustynski, *J. Am. Chem. Soc.* **107**, 2988–2990 (1985)
- M.M. Momeni, Y. Ghayeb, *Appl. Phys. A.* **122**, 620 (2016)
- R. Solarzka, R. Jurczakowski, J. Augustynski, *Nanoscale* **4**, 1553 (2012)
- D.-D. Qin, C.-L. Tao, S.A. Friesen, T.-H. Wang, O.K. Varghese, N.-Z. Bao, Z.-Y. Yang, T.E. Mallouk, C.A. Grimes, *Chem. Commun.* **48**, 729–731 (2011)
- J. Su, X. Feng, J.D. Sloppy, L. Guo, C.A. Grimes, *Nano Lett.* **11**, 203–208 (2010)
- S.S. Kalanur, Y.J. Hwang, S.Y. Chae, O.S. Joo, *J. Mater. Chem.* **1**, 3479–3488 (2013)
- S. Wang, H. Chen, G. Gao, T. Butburee, M. Lyu, S. Thaweesak, J.-H. Yun, A. Du, G. Liu, L. Wang, *Nano Energy* **24**, 94–102 (2016)
- Z. Jiao, J. Wang, L. Ke, X.W. Sun, H.V. Demir, *ACS Appl. Mater. Interfaces* **3**, 229–236 (2011)
- J. Yang, W. Li, J. Li, D. Sun, Q. Chen, *J. Mater. Chem.* **22**, 17744–17752 (2012)
- W. Li, C. Liu, Y. Yang, J. Li, Q. Chen, F. Liu, *Mater. Lett.* **84**, 41–43 (2012)
- Y. Li, X. Wei, X. Yan, J. Cai, A. Zhou, M. Yang, K. Liu, *Phys. Chem. Chem. Phys.* **18**, 10255–10261 (2016)
- Y. Liu, H. He, J. Li, W. Li, Y. Yang, Y. Li, Q. Chen, *RSC Adv.* **5**, 46928–46934 (2015)
- P. Chatchai, Y. Murakami, S.-Y. Kishioka, A.Y. Nosaka, Y. Nosaka, *Electrochim. Acta* **54**, 1147–1152 (2009)
- C. Liu, Y. Yang, W. Li, J. Li, Y. Li, Q. Chen, *Sci. Rep.* **6**, 23451 (2016)
- Z. Hu, M. Xu, Z. Shen, J.C. Yu, *J. Mater. Chem.* **3**, 14046–14053 (2015)
- F. Zhan, R. Xie, W. Li, J. Li, Y. Yang, Y. Li, Q. Chen, *RSC Adv.* **5**, 69753–69760 (2015)
- P.J. Barczuk, A. Krolikowska, A. Lewera, K. Miecznikowski, R. Solarzka, J. Augustynski, *Electrochim. Acta* **104**, 282–288 (2013)
- W. Li, J. Li, X. Wang, Q. Chen, *Appl. Surf. Sci.* **263**, 157–162 (2012)
- Y. Sun, C.J. Murphy, K.R. Reyes-Gil, E.A. Reyes-Garcia, J.M. Thornton, N.A. Morris, D. Raftery, *Int. J. Hydrogen. Energy* **34**, 8476–8484 (2009)
- W. Li, F. Zhan, J. Li, C. Liu, Y. Yang, Y. Li, Q. Chen, *Electrochim. Acta* **160**, 57–63 (2015)
- R. Solarzka, K. Bienkowski, S. Zoladek, A. Majcher, T. Stefaniuk, P.J. Kulesza, J. Augustynski, *Angew. Chem. Int. Ed. Engl.* **53**, 14196–14200 (2014)
- A. Phuruangrat, W. Kongpet, O. Yayapao, B. Kuntalue, S. Thongtem, T. Thongtem, *J. Nanomater.* **2014**, 1–10 (2014)
- A. Fujii, Z. Meng, C. Yogi, T. Hashishin, T. Sanada, K. Kojima, *Surf. Coat. Technol.* **271**, 251–258 (2015)
- F. Xu, Y. Yao, D. Bai, R. Xu, J. Mei, D. Wu, Z. Gao, K. Jiang, *RSC Adv.* **5**, 60339–60344 (2015)
- F. Le Formal, N. Tetreault, M. Cornuz, T. Moehl, M. Gratzel, K. Sivula, *Chem. Sci.* **2**, 737–743 (2011)
- X. Yang, R. Liu, C. Du, P. Dai, Z. Zheng, D. Wang, *ACS Appl. Mater. Interfaces* **6**, 12005–12011 (2014)
- Q. Gui, Z. Xu, H. Zhang, C. Cheng, X. Zhu, M. Yin, Y. Song, L. Lu, X. Chen, D. Li, *ACS Appl. Mater. Interfaces* **6**, 17053–17058 (2014)
- Y. Yang, R. Xie, Y. Liu, J. Li, W. Li, *Catalysts* **5**, 2024–2038 (2015)
- V.J. Angadi, A.V. Anupama, R. Kumar, H.M. Somashekarappa, K. Praveena, B. Rudraswamy, B. Sahoo, *Ceram. Int.* **42**, 15933–15939 (2016)
- Y. Liu, G. Liu, J. Wang, X. Dong, W. Yu, T. Wang, *J. Mater. Sci. Mater. Electron.* **27**, 10780–10790 (2016)
- C. Liu, C. Lyu, Y. Liu, Y. Lyu, *J. Mater. Sci. Mater. Electron.* **27**, 10473–10478 (2016)
- Y. Liu, J. Li, H. Tang, W. Li, Y. Yang, Y. Li, Q. Chen, *Electrochim. Commun.* **68**, 81–85 (2016)
- M.M. Mohamed, *J. Colloid Interface Sci.* **272**, 28–34 (2004)
- C.S. Blackman, I.P. Parkin, *Chem. Mater.* **17**, 1583–1590 (2005)

42. G.S. Smith, Q. Johnson, A.G. Tharp, *Acta Cryst.* **22**, 269–272 (1967)
43. W.J. Evans, I. Bloom, W.E. Hunter, J.L. Atwood, *J. Am. Chem. Soc.* **105**, 1401–1403 (1983)
44. A.A. Dakhel, *J. Alloys Compd.* **475**, 51–54 (2009)
45. A. Królikowski, E. Płońska, A. Ostrowski, M. Donten, Z. Stojek, *J. Solid State Electrochem.* **13**, 263–275 (2008)
46. G. Corbel, Y. Laligant, F. Goutenoire, E. Suard, P. Lacorre, *Chem. Mater.* **17**, 4678–4684 (2005)
47. H. Liao, L. Xie, Y. Zhang, X. Qiu, S. Li, Z. Huang, H. Hou, X. Ji, *Electrochim. Acta* **219**, 227–234 (2016)
48. L. Wei, Y. Yang, X. Xia, R. Fan, T. Su, Y. Shi, J. Yu, L. Li, Y. Jiang, *RSC Adv.* **5**, 70512–70521 (2015)
49. Y. Liu, J. Li, W. Li, H. He, Y. Yang, Y. Li, Q. Chen, *Electrochim. Acta* **210**, 251–260 (2016)
50. G. Cabello, A. Aranedá, L. Lillo, C. Caro, C. Venegas, M. Tejos, B. Chornik, *Solid State Sci.* **27**, 24–29 (2014)
51. S. Kundu, N. Sutradhar, R. Thangamuthu, B. Subramanian, A.B. Panda, M. Jayachandran, *J. Nanopart. Res.* **14**, 1–16 (2012)
52. A. Rydosz, A. Szkudlarek, M. Ziabka, K. Domanski, W. Maziarz, T. Pisarkiewicz, *IEEE Sens. J.* **16**, 1004–1012 (2016)
53. M. Khajeh Aminian, N. Taghavinia, A. Irajizad, S.M. Mahdavi, *J. Phys. Chem. C* **111**, 9794–9798 (2007)
54. Z. Li, J. Li, Y. Zhao, K. Yang, F. Gao, X. Li, *RSC Adv.* **6**, 15492–15500 (2016)
55. Y. Jung, R.A. Marcus, *J. Phys. Condens. Matter Inst. Phys. J.* **22**, 284117 (2010)
56. F. Chang, J. Wang, J. Luo, J. Sun, X. Hu, *J. Colloid Interface Sci.* **468**, 284–291 (2016)
57. S.K. Park, H.J. Lee, M.H. Lee, H.S. Park, *Chem. Eng. J.* **281**, 724–729 (2015)
58. K. Sivula, R. Van De Krol, *Nat. Rev. Mater.* **1**, 15010 (2016)
59. P. Sudhagar, A. Devadoss, K. Nakata, C. Terashima, A. Fujishima, *J. Electrochem. Soc.* **162**, H108–H114 (2015)
60. A.D. Walkingshaw, N.A. Spaldin, E. Artacho, *Phys. Rev. B* **70**, 165110 (2004)
61. P. Siriwong, T. Thongtem, A. Phuruangrat, S. Thongtem, *CrystrEngComm* **13**, 1564–1569 (2011)
62. T. Zhang, Z. Zhu, H. Chen, Y. Bai, S. Xiao, X. Zheng, Q. Xue, S. Yang, *Nanoscale* **7**, 2933–2940 (2015)
63. H. He, J. Huang, L. Cao, J. Wu, *Desalination* **252**, 66–70 (2010)
64. Y.A. Shaban, A.A. El Maradny, R.K. Al Farawati, *J. Photochem. Photobiol. A* **328**, 114–121 (2016)
65. L. Cui, X. Ding, Y. Wang, H. Shi, L. Huang, Y. Zuo, S. Kang, *Appl. Surf. Sci.* **391**, 202–210 (2016)
66. Y. Liu, J. Li, W. Li, Y. Yang, Y. Li, Q. Chen, *J. Phys. Chem. C* **119**, 14834–14842 (2015)
67. S. Hilaire, M.J. Suess, N. Kranzlin, K. Bienkowski, R. Solaraska, J. Augustynski, M. Niederberger, *J. Mater. Chem.* **2**, 20530–20537 (2014)